Zeeman splitting and g factor of the $1s^22s^22p\ ^2P_{3/2}$ and $^2P_{1/2}$ levels in Ar^{13+}

R. Soria Orts,[1] J. R. Crespo López-Urrutia,[1] H. Bruhns,[1] A. J. González Martínez,[1] Z. Harman,[1] U. D. Jentschura,[1] C. H. Keitel,[1] A. Lapierre,[1] H. Tawara,[1] I. I. Tupitsyn,[1,2] J. Ullrich,[1] and A. V. Volotka[2]
[1]*Max Planck Institute for Nuclear Physics, Saupfercheckweg 1, D 69117 Heidelberg, Germany*
[2]*Department of Physics, St. Petersburg State University, Oulianovskaya 1, Petrodvorets, 198504 St. Petersburg, Russia*
(Received 27 March 2007; published 5 November 2007)

The Zeeman line components of the magnetic-dipole ($M1$) $1s^22s^22p\ ^2P_{1/2}-^2P_{3/2}$ transition in boronlike Ar^{13+} were experimentally resolved by high-precision emission spectroscopy using the Heidelberg electron beam ion trap. We determined the gyromagnetic (g) factors of the ground and first-excited levels to be $g_{1/2}=0.663(7)$ and $g_{3/2}=1.333(2)$, respectively. This corresponds to a measurement of the g factor of a relativistic electron in a bound non-S state of a multielectron ion with a 1.5 parts-per-thousand accuracy. The results are compared to theoretical calculations by means of the configuration interaction Dirac-Fock-Sturmian method including electron correlation effects and additional quantum electrodynamic corrections. Our measurements show that the classical Landé g factor formula is sufficiently accurate to the present level of accuracy in few-electron ions of medium nuclear charge number Z.

DOI: 10.1103/PhysRevA.76.052501 PACS number(s): 31.30.Jv, 32.60.+i

I. INTRODUCTION

The prediction of the radiative correction to the electronic-spin g_s factor stimulated an increased interest in precision measurements of the atomic g_J factors some 50 years ago [1]. However, it was not straightforward to deduce the g_s factor from the measured g_J factor since a number of corrections had to be considered. These arose from the anomalous spin magnetic moment of the electron and relativistic and diamagnetic contributions to the linear Zeeman energies. A detailed theory of these corrections has been developed (see, e.g., Ref. [2]), but its application to a particular atom or ion is limited by the necessity of having accurate many-electron wave functions. Thus precisely measured atomic g_J factors are of special interest, allowing a sensitive test for the calculation of correlated wave functions. As another application, Shabaev *et al.* [3] proposed that the measurement of a specific difference of g_J factors in the H- and B-like charge state of the same heavy element may lead to a new determination of the fine-structure constant α.

Using the laser magnetic resonance technique, various g_J factor measurements have been performed by Abu Safia [4] in the lowest excited levels of Ne, Ar, Kr, and Xe and by Inguscio [5] in Si with an accuracy better than 10^{-4}. A recent experimental determination [6,7] by means of a Penning trap, in which a spin flip is directly excited, reached an accuracy of 10^{-9}. The g factor of the bound electron in the hydrogenlike ion O^{7+} has been found to be within 1.1 σ of the predicted theoretical value [8], representing a stringent test of bound-state quantum electrodynamics (QED) on a level of 0.25%. Assuming that the QED contributions are correct, the most precise value for the electron mass has been obtained this way. In addition, the experimental bound electron g factor can be used to determine other fundamental constants such as the fine-structure constant α, and to study properties of the atomic nucleus. It must be mentioned that, in order to achieve sufficient precision in the theoretical calculations, one has to account for the relativistic, one- and two-loop QED [8–10], nuclear size [11], nuclear recoil [12,13], and nuclear polarization corrections [14].

The magnetic interaction Hamiltonian is given in terms of the total orbital momentum $\boldsymbol{L}$ and spin operator $\boldsymbol{S}$ by (in atomic units, $\hbar=m_e=e=1$)

$$H_B=\mu_B(g_L\boldsymbol{L}+g_S\boldsymbol{S})\cdot\boldsymbol{B}, \tag{1}$$

where μ_B is the Bohr magneton, $\boldsymbol{B}$ the external magnetic field, and g_L and g_S are the orbital and spin g factors, respectively. In the case of a weak field, the Zeeman splitting [15] is small compared to the fine-structure splitting which is proportional to the internal magnetic field B_{int} of the atom and first-order perturbation theory can be applied. The Zeeman energy shift of an atomic state $|\Gamma LSJM_J\rangle$ can then be written as

$$\Delta E=\langle\Gamma LSJM_J|g_J\mu_B B\hat{J}_z|\Gamma LSJM_J\rangle=g_J\mu_B BM_J, \tag{2}$$

where M_J is the projection of the total angular momentum J on the z axis and g_J is the Landé factor of the electronic state. Γ is a multi-index summarizing the orbital occupation and coupling scheme of the many-electron state. For the general case of transitions between multiplets in LS coupling, g_J depends on the quantum numbers L, S, and J and, hence, is different for each level (anomalous Zeeman effect). The modified frequency ν of a transition $|\Gamma LSJM_J\rangle \rightarrow|\Gamma' L'S'J'M_{J'}\rangle$ is given by

$$h\nu=(E'+\Delta E')-(E+\Delta E)=h\nu_0+\mu_B B(g_{J'}M_{J'}-g_JM_J), \tag{3}$$

where h is the Planck constant and ν_0 corresponds to the unperturbed transition frequency.

We have determined the g_J factors of the $1s^22s^22p\ ^2P_{3/2}$ and $^2P_{1/2}$ fine-structure levels in boronlike Ar^{13+} through precision measurements of the Zeeman patterns and the transition wavelengths of the magnetic dipole $M1$ transitions between the levels. It has been known for a long time that $M1$ forbidden transitions, first identified by Edlén [16], between the fine-structure levels of multiply charged ions are the origin of many of the solar coronal lines and play a vital role in

studies of the temperature and density of solar plasmas [17,18]. Very recently, the Zeeman spectral line profiles of magnetic dipole transitions in Ar^{9+}, Ar^{10+}, Ar^{13+}, and Ar^{14+} have been measured in the large helical device [19]. In particular, the boronlike isoelectronic sequence is one of the simplest with such a fine-structure transition in the ground term, featuring a single line. For ions with nuclear charge numbers in the range between approximately 10 and 20, this line appears in the visible spectrum, where spectroscopic techniques are capable of achieving very accurate measurements. For example recently, the lifetime of the metastable $^2P_{3/2}$ state was determined with a 10^{-3} accuracy to be 9.573(4)(5) ms [20]. As the optical electron active in this transition has a binding energy of the order of several hundreds of eVs, relativistic effects are essential. The electron is also much closer to the nucleus than typical valence electrons associated with optical transitions in neutral atoms and low charge state ions. This strong overlap of the electron wavefunction with the nucleus results in significant QED contributions to the transition energy (up to 1%). Therefore the forbidden lines are very well-suited to study these effects since their relative contribution to the wavelength λ is rather large in comparison to the expected experimental error bar [21]. The present spectroscopic studies of forbidden $M1$ transitions in highly charged ions were carried out by finding particularly favorable conditions at the Heidelberg electron beam ion trap (EBIT). The final results are compared with large-scale configuration-interaction (CI) Dirac-Fock-Sturmian (DFS) calculations also containing QED contributions.

II. EXPERIMENTAL SETUP AND METHOD

One of the most serious problems in the Zeeman splitting measurements, particularly for heavy ions, arises from the fact that in nearly all cases the level splitting is small compared with the experimentally observed linewidth. In order to reduce the linewidth due to the Doppler broadening, the ion temperatures have to be reduced significantly.

The present experiment was performed at the EBIT of the Max-Planck-Institut für Kernphysik in Heidelberg [22]. Argon gas was injected into the trap region as a low-density atomic beam and, through stepwise collisional ionization by the high-density electron beam, highly charged Ar^{13+} ions were efficiently produced. The evaporative cooling of these trapped ions was achieved by a proper choice of the trap parameters in the EBIT. Low primary electron current (typically 20 mA) reduced the Coulomb heating of the trapped ions and the gradients of the electrostatic trapping field originated by the space charge of the electron beam in comparison with an earlier measurement at the electron beam current $I_e = 100$ mA [21].

Another essential point to reduce the ion temperature was to use a very low axial trapping voltage of nominally 0–10 V during the observation, which is externally superimposed to the intrinsic longitudinal space charge potential (estimated to be about 10 V under the present EBIT conditions) in combination with a relatively low electron beam energy of $E_e \approx 700$ eV, which was just sufficient to produce Ar^{13+} ions.

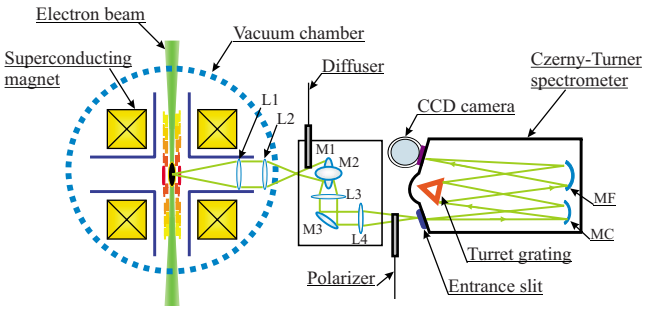

FIG. 1. (Color online) Sketch of the setup used in the present experiment. Two quartz lenses (L1 and L2) are installed inside the main vacuum chamber. Outside the EBIT, the light passes through an optical system (including the mirrors M1, M2, and M3, and the lenses L3 and L4) into the Czerny-Turner spectrometer. MC and MF are two mirrors, which collimate and focus the light, respectively.

The axial trapping voltage can be controlled by varying the voltages applied to the drift tubes. In addition, the intrinsic axial space charge potential due to the difference in the diameters between the central drift tube and the outer drift tubes, which is proportional to the electron beam current, was also reduced as the beam intensity was lowered. By choosing a low trapping potential, the fraction of hot ions in the Maxwell-Boltzmann velocity distribution capable of leaving the trap is increased, resulting in a higher evaporation rate and a lowering of the temperature of the remaining trapped ions. Through such effective control of the evaporation rate, the observed Doppler linewidth [full width at half maximum (FWHM)] could be reduced to 0.013 nm for the Ar line at 441.25 nm, while the 6.820 T magnetic field generated a splitting of 0.0414 nm for the central Zeeman components (for more details see below).

The optical setup used in the experiment is shown in Fig. 1. The optical access to the EBIT is provided through a quartz window on a side vacuum port. In order to obtain a real image of the trapped ions at the outside of the EBIT, two lenses (L1 and L2) are mounted inside the main vacuum chamber. Three mirrors and two additional lenses are used to rotate the horizontal image of the trapped ions and to project it onto a vertical entrance slit (nominally 50 μm) of a Czerny-Turner spectrometer. The spectrometer has a 2400 lines/mm grating which was used in the first order, yielding the linear dispersion of approximately 0.009 nm/pixel over the 18 nm spectral range on the cooled charge coupled device (CCD) camera. The CCD camera was divided into eight regions in the nondispersive direction and only the pixels located at the central 4.5 mm (300 pixels) strip on the CCD camera were used for the data analysis. Thus coma and other nonparaxial aberrations causing deviations from a symmetric line profile were minimized. The relative grating efficiency was measured to be 60% at 442 nm. Its efficiency was different for the two linear—parallel (π) and perpendicular (σ)—polarizations in relation to the grating ruling orientation. The ratio of both efficiencies was measured to be $A(\pi)/A(\sigma) = 0.46$. Data acquisition and spectrometer manipulation were controlled using the Jobin-Yvon SpectraMax software (version 3.0).

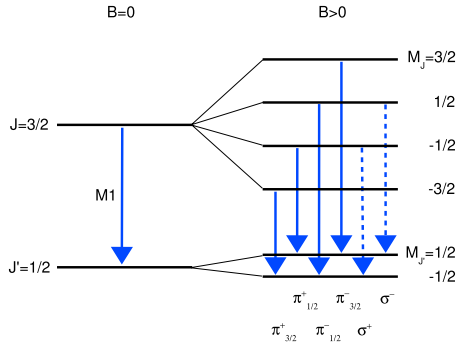

FIG. 2. (Color online) Zeeman splitting level diagram of the $1s^22s^22p\ ^2P_{3/2}$ and $^2P_{1/2}$ levels in Ar^{13+}. Under the presence of the magnetic field ($B \neq 0$, right figure), the π ($\Delta M_J = \pm 1$, solid lines) and σ ($\Delta M_J = 0$, dashed lines) transition components can be observed. The energy separations are not to scale.

For the wavelength calibration of the spectrometer, an iron hollow cathode lamp was used. About ten well-established lines from the NIST database [23] were chosen over the range of our interest. All of the recorded profiles of these lines have been found to be Gaussian. Their wavelengths were plotted against the peak pixel position and fitted by a second-order polynomial function in order to determine the instrumental dispersion curve. The instrumental response profile (W_r) of the spectrometer was determined to be 0.019(1) nm. The calibration was repeated before and after each measurement of the Ar lines in order to check the stability of the whole optical system. During this time, two successive measurements were made for each Ar^{13+} spectrum as well as for the calibration spectrum to remove spikes due to cosmic rays and also to correct the readout noise. The data acquisition times were about 30 min for the argon ion lines and 15 min for the calibration. The Ar^{13+} ion line observations were repeated 30–40 times, each time slightly changing the grating position (by 0.05 nm) to minimize possible uncertainties in binning of the pixels. When the linewidth is reduced to a few pixels, the determination of the line centroid can become more problematic, as a certain number of data points is required to sample it. By scanning the grating position, the line (which has a FWHM of only a few pixels on the CCD detector) is projected on different sections of the focal plane detector. Since each of these spectra was calibrated individually, we were able to determine the line centroid positions with an accuracy of approximately 0.3 pixels corresponding to a wavelength uncertainty of 2.7×10^{-4} nm ($\approx$1 ppm). Various effects like background and coma aberration which otherwise could affect the line shape and cause deviations of the line profile from an ideal Gaussian shape were checked varying the fitting intervals around the line.

III. DATA ANALYSIS AND RESULTS

According to the selection rules, we expect six emission lines from the transitions involving the split $^2P_{3/2}$-$^2P_{1/2}$ levels (see Fig. 2). Indeed, they were clearly observed as shown in Fig. 3 which was taken under the conditions of $I_e = 20$ mA, $E_e = 875$ eV (space charge corrected), and $B = 6.820$ T (without a polarizer). Six Gaussians were fitted to the observed spectrum, assuming that these six components had the same FWHM at their positions.

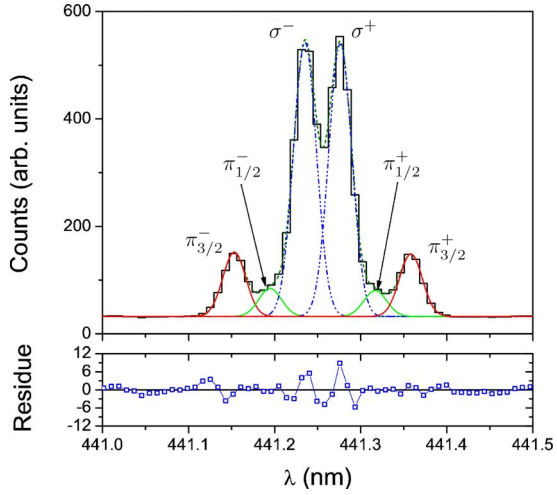

FIG. 3. (Color online) Typical spectrum of the $^2P_{1/2}$-$^2P_{3/2}$ line in Ar^{13+}, observed at $E_e = 875$ eV, $I_e = 20$ mA, and $B = 6.820$ T without a polarizer. The six dashed curves are fits to the Zeeman components. For the notation of the π and σ component labels, see the text and Fig. 2. The lower plot shows the fitting residue.

The light emitted in these transitions is linearly polarized according to the inclination angle between the magnetic field and viewing direction and the magnetic quantum number M_J involved in the transition. In the transversal view to the magnetic field axis, the central σ components ($\Delta M_J = 0$) of these $M1$ transitions are linearly polarized perpendicular to the field, meanwhile the outer π components ($\Delta M_J = \pm 1$) are linearly polarized parallel to the field. (We note that the polarization follows a different pattern in the case of $E1$ transitions.) Therefore, by using a polarizer, we were able to separate the σ and π components in both polarization directions. Such polarized spectra, taken with a 20 mA/700 eV electron beam under a magnetic field of 6.820 T, are shown in Fig. 4. In Fig. 4(a) the four π components are clearly resolved, meanwhile Fig. 4(b) shows the two σ components. It is clear that, by separating the components with different polarization, the lines appear better resolved, as the residual plots show.

A. Temperature of the trapped ions

In any spectral observation, it is important to minimize the line broadening due to the temperature of the species under investigation. The ion temperature T_i, assuming a Maxwellian distribution, is related to the Doppler broadening with a Gaussian width W_D by the following relation:

$$T_i = \frac{M_i c^2}{8 k_B \ln 2} \left(\frac{W_D}{\lambda_0} \right)^2, \tag{4}$$

where λ_0 corresponds to the central wavelength (at $B = 0$), k_B is the Boltzmann constant, M_i is the atomic mass of the ion, and c is the speed of light.

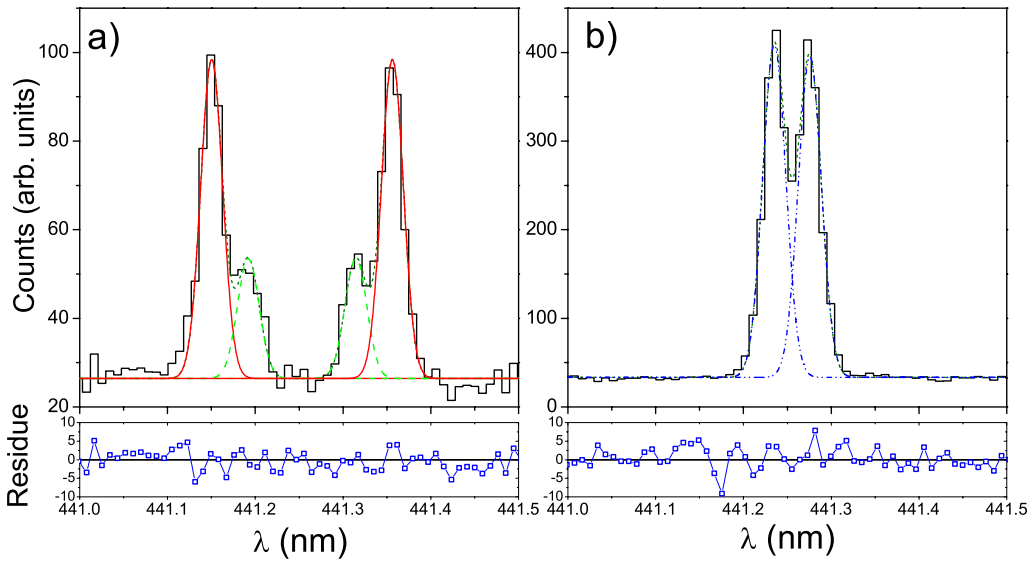

FIG. 4. (Color online) Spectra of (a) π and (b) σ Zeeman components of $M1$ transitions of Ar^{13+} ions at E_e=700 eV, I_e=20 mA, and B=6.820 T, separated with a polarizer. The lower plots show the fitting residues.

The observed linewidth W_o includes not only the natural transition linewidth W_i, which is negligibly small in the case of these forbidden transitions, but also the instrumental broadening W_r due to the spectrometer finite resolution as well as the Doppler broadening W_D due to the ionic motion. Since the distributions originating from these two largest contributing effects, W_D and W_r, are well-described by Gaussian functions, the convolution of the two is expected to yield a Gaussian profile, of which the width can be calculated. Thus the Doppler broadening is given as $W_D = \sqrt{W_o^2 - W_r^2}$. Note that W_r is 0.019(1) nm, as mentioned above.

The results for the ion temperatures obtained at two different electron beam currents I_e, keeping other EBIT parameters unchanged, are listed in Table I. The uncertainties given are the quadratic sum of all uncertainties involved. It is clear that, by reducing the electron beam current from I_e=50 to 20 mA, the trapped ion temperature significantly decreased from 21 to 7 eV (see Table I). On the other hand, the count rate became smaller and, therefore, the statistical errors larger. This problem affects especially the weak π components, as we cannot completely separate the four lines, and so the errors in the determination of their position and width were larger. In the case of the σ components, as only two components do appear, the fits determined the linewidth with an error smaller than 4% of the total width.

It should be emphasized that such low ion temperatures have not been reported in an EBIT. This can clearly be in part due to less collisional heating by electrons and in part due to the lower axial potential, resulting in an enhanced evaporative cooling, and $W_o \approx 0.013$ nm at a wavelength of 441 nm corresponds to $\lambda/\delta\lambda \approx 34\,000$.

B. Determination of the central wavelength

From the six Gaussian functions used to fit the spectra as shown in Figs. 3 and 4, three independent results of the central wavelength λ_0 can be obtained. In order to minimize the uncertainty, the central wavelength from a pair of these six emission lines was obtained as follows:

TABLE I. Observed linewidths W_o and calculated Doppler widths W_D, as well as ion temperatures for different electron beam currents at E_e=700 eV and B=6.820 T. The values denoted by "Unpolarized" were obtained through measurements without a polarizer (see Fig. 3). On the other hand, for the other two cases, π and σ component observations, the polarizer was used and the parameters were determined independently (see Fig. 4). The row denoted by "Average" shows the average values.

	I_e=50 mA			I_e=20 mA		
	W_o (nm)	W_D (nm)	T_i (eV)	W_o (nm)	W_D (nm)	T_i (eV)
Unpolarized	0.031(1)	0.024(1)	20(2)	0.023(1)	0.013(1)	6(1)
π	0.031(3)	0.024(3)	20(5)	0.023(2)	0.013(2)	6(2)
σ	0.032(1)	0.026(1)	23(2)	0.024(1)	0.015(1)	8(1)
Average		0.0249(7)	21.4(1.4)		0.0139(7)	6.9(7)

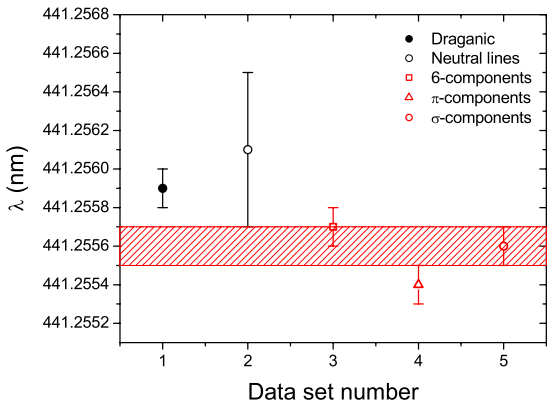

FIG. 5. (Color online) Comparison of the present results of the central wavelength λ_0 with those of a previous experiment (closed symbol, Draganić *et al.*, Ref. [21]), and another value obtained with the calibration made using Ar I and Ar II lines ("neutral lines"). In the present experiment (open symbols), the magnetic field was $B=6.820$ T. The shadowed area represents the average value and the uncertainties of the present result. The closed symbol corresponds to the previous measurement [21] where the Doppler broadening smeared out the Zeeman splitting and, hence, the spectrum was fitted with a single Gaussian function. Note that the previous data point (closed symbol) was obtained at $B=5.25$ T.

$$\lambda_0(k) \equiv \frac{\lambda(k^+) + \lambda(k^-)}{2}, \tag{5}$$

where $\lambda(k^+)$ and $\lambda(k^-)$ correspond to the wavelengths of the up- and down-shifted peaks due to the magnetic field, respectively. k represents a particular transition line of the π and σ components (see Fig. 2). The average wavelength λ_0 among π and σ transitions in Fig. 3 (without distinguishing the polarization) has been found to be 441.2557(1) nm. Similar measurements were repeated separately for the π and σ components by using the polarizer. From the σ components the resulting wavelength is 441.2556(1) nm and, from the π components is 441.2554(1) nm. Note that the uncertainties of the calibration lines are of the order of 10^{-4} to 10^{-5} nm. As every calibration used several reference lines and, thus, the calibration uncertainties were rather small, the total error is determined mainly by the statistical uncertainties of the peak position determination of the Zeeman components. The reproducibility of the results over 40 different points results in an uncertainty of the averaged wavelength smaller than 0.3 ppm, yielding the final value of 441.2556(1) nm.

In Fig. 5 the results obtained in the present work (open marks) are compared to previous experiments which include a result by Draganić [21] and another independent value obtained with the *in situ* calibration made using Ar I and Ar II lines excited in the EBIT ("neutral lines" in Fig. 5). In all these cases, λ_0 was determined from the spectrum obtained without a polarizer assuming a single Gaussian profile. The slight disagreement with the result in the case of the Ar^{13+} line may be explained by the use of a different set of calibration lines. (For another transition in Ar^{14+} the agreement was perfect.) The hollow cathode lamp utilized here is believed to deliver more reliable, narrower lines than those of the calibration lamps used in [21].

C. Determination of the g factors

It is expected that the six emission lines observed in the spectrum for the $^2P_{1/2}$-$^2P_{3/2}$ transitions of Ar^{13+} ions under the present experimental conditions are almost equally separated from each other. The energy of the transition from the magnetic sublevel $E(J,M_J)$ to $E(J',M_{J'})$ is related to the observed line separation [wavelength difference $\Delta\lambda(k) = \lambda(k^+) - \lambda(k^-)$, see Fig. 2] by the following equations:

$$\Delta\lambda(\pi_{3/2}) = \frac{\lambda_0^2}{hc}\left[\Delta E\left(\tfrac{3}{2},\tfrac{3}{2}\right) - \Delta E\left(\tfrac{1}{2},\tfrac{1}{2}\right)\right],$$

$$\Delta\lambda(\pi_{1/2}) = \frac{\lambda_0^2}{hc}\left[\Delta E\left(\tfrac{3}{2},\tfrac{1}{2}\right) + \Delta E\left(\tfrac{1}{2},\tfrac{1}{2}\right)\right],$$

$$\Delta\lambda(\sigma) = \frac{\lambda_0^2}{hc}\left[\Delta E\left(\tfrac{3}{2},\tfrac{1}{2}\right) - \Delta E\left(\tfrac{1}{2},\tfrac{1}{2}\right)\right]. \tag{6}$$

Here $\Delta E(J,M_J)$ represents the shift of the originally degenerate energy level $E(J)$ under the influence of the magnetic field B: $\Delta E(J,M_J) = E(J,M_J) - E(J)$. Thus they are given as follows:

$$\Delta E\left(\tfrac{3}{2},\tfrac{3}{2}\right) = \left[\frac{\Delta\lambda(\pi_{1/2}) - \Delta\lambda(\sigma)}{2} + \Delta\lambda(\pi_{3/2})\right]\frac{hc}{\lambda_0^2},$$

$$\Delta E\left(\tfrac{1}{2},\tfrac{1}{2}\right) = \left[\frac{\Delta\lambda(\pi_{1/2}) - \Delta\lambda(\sigma)}{2}\right]\frac{hc}{\lambda_0^2}. \tag{7}$$

Hence combining with Eq. (3), the g_J factors are expressed as

$$g_{3/2} = \frac{\Delta E\left(\frac{3}{2},\frac{3}{2}\right)}{\frac{3}{2}\mu_B B},$$

$$g_{1/2} = \frac{\Delta E\left(\frac{1}{2},\frac{1}{2}\right)}{\frac{1}{2}\mu_B B}. \tag{8}$$

Based upon the observed Zeeman splitting (see Figs. 3 and 4) of the transition lines under the present magnetic field, we were able to determine their g_J factors using Eq. (8) shown above. The final g_J factors are shown in Table II (last column), together with theoretical contributions. The experimental uncertainties are estimated from the quadratic sum of the relevant errors. As Eq. (8) shows, the uncertainty of the magnetic field strength determination contributes to this error balance.

The g_D corresponds to the one-electron Dirac g factor, Δg_{corr} is the correction due to the interelectronic correlation, and Δg_{neg} is the contribution of the negative continuum spectrum. These two terms were calculated with a CI method using Dirac-Fock-Sturmian wave functions. Δg_{QED} represents the QED correction. (See the next section for further

TABLE II. Various contributions to the g factor g_{total} calculated with the CI DFS method in comparison with the experimental result g_{expt}. The symbol g_{NR} stands for the nonrelativistic Landé g factor, g_{D} is the relativistic Dirac value, Δg_{corr} represents the electron correlation correction, Δg_{neg} is the contribution of the negative part of the continuous spectrum, and Δg_{QED} denotes QED corrections to the g factor. See text for further details.

Level	g_{NR}	g_{D}	Δg_{corr}	Δg_{neg}	Δg_{QED}	g_{total}	g_{expt}
$^2P_{1/2}$	0.6666667	0.6637754	0.0006943	−0.0000425	−0.00078	0.66365	0.663(7)
$^2P_{3/2}$	1.3333333	1.3310304	0.0005443	−0.0000613	0.00077	1.33228	1.333(2)

details.) The present experimental data for both $^2P_{1/2}$ and $^2P_{3/2}$ states seem to be in good agreement with the total theoretical values. However, it is clear that the accuracy of the current experiment is not sufficient to test the various physical contributions.

IV. CALCULATION OF g FACTORS

We carried out a fully relativistic calculation of the bound electron g factors. In the zeroth-order approximation, the interaction of the $2p$ electron with the closed K shell and the closed $2s$ subshell is neglected. Thus the one-electron Dirac equation with the Hamiltonian

$$h = c\boldsymbol{\alpha}\cdot\boldsymbol{p} + \beta c^2 + V_{\text{nuc}} + V_{\text{magn}} \tag{9}$$

can be used. Here, V_{nuc} is the nuclear Coulomb potential and $V_{\text{magn}} = \boldsymbol{\alpha}\cdot\boldsymbol{A} = \frac{1}{2}\boldsymbol{B}\cdot(\boldsymbol{r}\times\boldsymbol{\alpha})$ describes the interaction with the homogeneous external magnetic field, and $\boldsymbol{\alpha}$ and β are the usual Dirac matrices acting on the four-component wave functions.

A calculation of the energy shift due to V_{magn} in first order using analytic Dirac (D) wave functions corresponding to a pointlike nucleus yields the lowest-order g factor, namely [24],

$$g_{\text{D}} = \frac{\kappa}{j(j+1)}\left(\kappa\frac{\gamma+n-|\kappa|}{\sqrt{(\gamma+n-|\kappa|)^2+(\alpha Z)^2}} - \frac{1}{2}\right). \tag{10}$$

Here, n, l, j, and $\kappa=(j+1/2)(-1)^{j+l+1/2}$ are the principal quantum number, the orbital and total angular momentum, and the relativistic angular quantum number of the one-electron state, respectively. Z is the nuclear charge number and $\gamma=\sqrt{\kappa^2-(\alpha Z)^2}$. Formula (10) reduces in the nonrelativistic (NR) limit $\alpha\to 0$ to the Landé formula

$$g_{\text{NR}} = 1 + \frac{j(j+1) - l(l+1) + 3/4}{2j(j+1)}, \tag{11}$$

which does not depend on Z and n.

For a general many-electron atomic state Ψ with the maximal projection of the total angular momentum ($J=M_J$), the g factor is defined as

$$g = \frac{1}{\mu_B M_J}\left.\frac{\partial}{\partial B}\langle\Psi|H|\Psi\rangle\right|_{B=0}. \tag{12}$$

The total relativistic Hamiltonian H contains the sum of one-electron operators [Eq. (9)] and the Coulomb and Breit electron interaction operators in the no-pair approximation.

In the configuration interaction (CI) method applied here, the many-electron wave function Ψ is expanded in terms of Slater determinants with the same projection M_J:

$$\Psi(M_J) = \sum_i c_i(M_J)\det{}_i(M_J). \tag{13}$$

The Slater determinants in turn are constructed from one-electron wave functions that are determined in the following way: the orbitals corresponding to occupied $1s$, $2s$, and $2p$ subshells were generated by the restricted Dirac-Fock method, and vacant correlation orbitals were obtained by numerically solving the Dirac-Fock-Sturm equations. This procedure was applied recently to calculate the electron interaction correction to the g factor of Li-like ions in Ref. [9], where more details can be found. The correlated many-electron wave functions thus obtained are used to calculate the g factor corresponding to the boronlike states by a finite-difference approximation [9] of Eq. (12) in the variable B. Electron correlation corrections (Δg_{corr}), together with the contribution of negative-energy states calculated by means of perturbation theory (Δg_{neg}) are given in Table II.

The QED correction to the g factor of boronlike ions is given by the one-electron QED contribution of the $2p_{1/2}$ and $2p_{3/2}$ states, when neglecting electron interaction (screening) effects. In the present work we evaluated the self-energy and vacuum polarization corrections in the first order of the fine-structure constant α, with methods described in [9] and references therein. The result for the QED contribution Δg_{QED} is presented in Table II.

The correction to the g-factor value due to the finite size of the nucleus can be calculated by a closed formula in Ref. [11]. Given the present experimental accuracy, this effect is found to be negligible for our system. Similarly, nuclear recoil [12] and nuclear polarization [14] effects can be neglected at the current experimental accuracy, too.

V. CONCLUSION

We have succeeded in reducing the ion temperatures in the EBIT down to 7 eV by means of evaporative cooling. Such a reduction of the Doppler broadening allowed us to determine the central (magnetic field-free) wavelength of the $1s^22s^22p\ ^2P_{1/2}-{}^2P_{3/2}$ transition of highly ionized Ar^{13+} ions to be 441.2556(1) nm and to observe the Zeeman splitting of this line. From this splitting, we have determined the g_J factors for the $^2P_{1/2}$ and $^2P_{3/2}$ levels to be $g_{1/2}=0.663(7)$ and

$g_{3/2}=1.333(2)$, respectively. To the best of our knowledge, the achieved 1.5 parts-per-thousand accuracy of determining the g factor of a bound electron in a P state of a few-electron highly charged ion is unprecedented. Our experimental results are found to be in good agreement with theoretical predictions based on the CI DFS method within the experimental uncertainties. We found that on the present 10^{-3} accuracy level, a one-electron quantum calculation is still sufficient for the description of the bound electron g factor.

New ion cooling schemes under development aim at reaching lower trapped ion temperatures, which combined with, e.g., two-photon Doppler-free laser spectroscopy may achieve an accuracy close to that already reached by the continuous Stern-Gerlach effect (CSG) method in Penning traps (see, e.g., Ref. [25]). The advantage of laser spectroscopy is that it can also access excited states, while the CSG technique can only address the electronic ground state. These anticipated improvements in the accuracy are expected to provide a strong basis to test correlation and QED contributions on the P-state g factor and thus open new experimental possibilities to study magnetic effects in the spectra of highly charged many-electron ions.

[1] R. Beringer and M. A. Heald, Phys. Rev. **95**, 1474 (1954).
[2] L. Veseth, Phys. Rev. A **22**, 803 (1980).
[3] V. M. Shabaev, D. A. Glazov, N. S. Oreshkina, A. V. Volotka, G. Plunien, H. J. Kluge, and W. Quint, Phys. Rev. Lett. **96**, 253002 (2006).
[4] H. Abu Safia, J. P. Grandin, and X. Husson, J. Phys. B **14**, 3363 (1981).
[5] M. Inguscio, V. Beltrán López, and E. Ley-Koo, Astrophys. J. **278**, L127 (1984).
[6] J. Verdú, S. Djekić, H. Haffner, S. Stahl, T. Valenzuela, M. Vogel, G. Werth, H.-J. Kluge, and W. Quint, Phys. Rev. Lett. **92**, 093002 (2004).
[7] M. Vogel, J. Alonso, S. Djekić, H.-J. Kluge, W. Quint, S. Stahl, J. Verdú, and G. Werth, Nucl. Instrum. Methods Phys. Res. B **235**, 7 (2005).
[8] V. A. Yerokhin, P. Indelicato, and V. M. Shabaev, Phys. Rev. Lett. **89**, 143001 (2002).
[9] D. A. Glazov, V. M. Shabaev, I. I. Tupitsyn, A. V. Volotka, V. A. Yerokhin, G. Plunien, and G. Soff, Phys. Rev. A **70**, 062104 (2004).
[10] K. Pachucki, A. Czarnecki, U. D. Jentschura, and V. A. Yerokhin, Phys. Rev. A **72**, 022108 (2005).
[11] D. A. Glazov and V. M. Shabaev, Phys. Lett. A **297**, 408 (2002).
[12] V. M. Shabaev, Phys. Rev. A **64**, 052104 (2001).
[13] V. M. Shabaev and V. A. Yerokhin, Phys. Rev. Lett. **88**, 091801 (2002).
[14] A. V. Nefiodov, G. Plunien, and G. Soff, Phys. Rev. Lett. **89**, 081802 (2002).
[15] P. Zeeman, Philos. Mag. **46**, 226 (1897).
[16] B. Edlén, Z. Astrophys. **22**, 30 (1942).
[17] U. Feldman, Phys. Scr. **24**, 681 (1981).
[18] S. V. Berdyugina and S. K. Solanki, Astron. Astrophys. **385**, 701 (2002).
[19] A. Iwamae, M. Atake, A. Sakaue, R. Katai, M. Goto, and S. Morita, Phys. Plasmas **14**, 042504 (2007).
[20] A. Lapierre *et al.*, Phys. Rev. Lett. **95**, 183001 (2005).
[21] I. Draganić, J. R. Crespo López-Urrutia, R. DuBois, S. Fritzsche, V. M. Shabaev, R. S. Orts, I. I. Tupitsyn, Y. Zou, and J. Ullrich, Phys. Rev. Lett. **91**, 183001 (2003).
[22] J. R. Crespo López-Urrutia, B. Bapat, I. Draganić, A. Werdich, and J. Ullrich, Phys. Scr., T **92**, 110 (2001).
[23] See the URL http://physics.nist.gov.
[24] S. A. Zapryagaev, Opt. Spektrosk. **47**, 18 (1979); Opt. Spectrosc. **47**, 9 (1979).
[25] N. Hermanspahn, H. Häffner, H. J. Kluge, W. Quint, S. Stahl, J. Verdú, and G. Werth, Phys. Rev. Lett. **84**, 427 (2000).